





# Laboratory Observations of Ultra-low-frequency Analog Waves Driven by the Right-hand Resonant Ion Beam Instability

Peter V. Heuer<sup>1</sup> , Martin. S. Weidl<sup>1,4</sup>, Robert S. Dorst<sup>1</sup>, Derek B. Schaeffer<sup>1,5</sup>, Shreekrishna K. P. Tripathi<sup>1</sup>, Stephen Vincena<sup>1</sup>, Carmen G. Constantin<sup>1</sup>, Christoph Niemann<sup>1</sup>, Lynn B. Wilson III<sup>2</sup> , and Dan Winske<sup>3</sup>

<sup>1</sup> Department of Physics and Astronomy, University of California-Los Angeles, Los Angeles, CA 90095, USA; [pheuer@physics.ucla.edu](mailto:pheuer@physics.ucla.edu), [cniemann@g.ucla.edu](mailto:cniemann@g.ucla.edu)

<sup>2</sup> NASA Goddard Space Flight Center, Greenbelt, MD 20771, USA

<sup>3</sup> Los Alamos National Laboratory, Los Alamos, New Mexico 87544, USA

Received 2019 December 12; revised 2020 February 11; accepted 2020 February 13; published 2020 February 27

## Abstract

The right-hand resonant instability (RHI) is one of several electromagnetic ion/ion beam instabilities responsible for the formation of parallel magnetized collisionless shocks and the generation of ultra-low frequency (ULF) waves in their foreshocks. This instability has been observed for the first time under foreshock-relevant conditions in the laboratory through the repeatable interaction of a pre-formed magnetized background plasma and a super-Alfvénic laser-produced plasma. This platform has enabled unprecedented volumetric measurements of waves generated by the RHI, revealing filamentary current structures in the transverse plane. These measurements are made in the plasma rest frame with both high spatial and temporal resolution, providing a perspective that is complementary to spacecraft observations. Direct comparison of data from both the experiment and the *Wind* spacecraft to 2D hybrid simulations demonstrates that the waves produced are analogous to the ULF waves observed upstream of the terrestrial bow shock.

*Unified Astronomy Thesaurus concepts:* [Laboratory astrophysics \(2004\)](#); [Planetary bow shocks \(1246\)](#); [Space plasmas \(1544\)](#); [Plasma astrophysics \(1261\)](#); [Shocks \(2086\)](#)

## 1. Introduction

Parallel magnetized collisionless shocks, including terrestrial (Turner et al. 2018), cometary (Tsurutani 2013), other planetary bow shocks (Hoppe & Russell 1981) and supernovae (Gargaté & Spitkovsky 2011), are objects of considerable interest (Burgess et al. 2012; Burgess & Scholer 2012) due to their ability to accelerate high-energy cosmic rays (Blandford & Eichler 1987; Caprioli & Spitkovsky 2014) and cyclically reform (Burgess 1989). Collisionless shocks are discontinuities formed by the collisionless interaction of a super-Alfvénic inflowing plasma and a magnetized ambient plasma. As inflowing ions pass through the shock, they are slowed and heated. A parallel shock is the region of a shock where the inflowing plasma streams nearly parallel to the background magnetic field. In this region some inflowing ions are shock-reflected back upstream (Onsager et al. 1991), forming an extended foreshock region (Eastwood et al. 2005). The parallel foreshock is dominated by ultra-low frequency (ULF) waves with frequencies near the ion cyclotron frequency (Hoppe et al. 1982; Greenstadt et al. 1995). These waves thermalize the reflected ions through pitch-angle scattering forming the “intermediate” ion distribution (Fuselier 1995). These ions and ULF waves then convect back into the shock, coupling the shock and foreshock regions (Burgess 1995) and playing an important role in shock re-formation (Winske et al. 1990; Scholer & Burgess 1992). ULF waves are responsible for a variety of foreshock structures including shocklets (Hada et al. 1987) and filaments in the magnetic field, density, and temperature (Wang & Lin 2006; Omididi et al. 2014). Many spacecraft and simulations have observed these waves, but

none have resolved their three-dimensional structure with high resolution. The spatial features of these waves, and the ways in which these features influence the formation of foreshock structures, remain open questions.

ULF waves in the foreshock are driven by the right-hand resonant instability (RHI), an electromagnetic ion/ion beam instability that develops between the super-Alfvénic shock-reflected “beam” ions and the ambient inflowing “core” ions (denoted  $c$  and  $b$ , respectively) (Jeffrey 2013). The RHI is a gyro-resonant interaction between the core and beam ions that leads to the growth of a large-amplitude, right-hand circularly polarized electromagnetic wave on the whistler/magnetosonic branch of the cold-beam dispersion relation (Montgomery et al.

1975; Gary 1991; Weidl et al. 2019a). The RHI dominates when the beam ion density  $n_b$  is much less than the core ion density  $n_c$  and the Alfvénic Mach number  $M_A = v_b/v_A$  is in the range  $2 < M_A < 10$ . Here,  $v_b$  is the beam ion velocity and  $v_A = B_0/\sqrt{\mu_0 n_c m_c}$  is the Alfvén velocity in the core plasma ( $B_0$  is the magnitude of the background magnetic field,  $\mu_0$  is the permeability of free space, and  $m_c$  is the core ion mass). At high beam densities and velocities within this range, the RHI growth rate  $\gamma_{\text{RHI}}(k)$  bifurcates (Weidl et al. 2019a), producing a second peak at higher frequency called the “electron-ion whistler instability” (Akimoto et al. 1987). At beam densities and velocities above this range, another instability called the non-resonant instability (NRI) outgrows the RHI (Gary 1991; Weidl et al. 2019b). Working together, the RHI and NRI form a parallel shock (Golden et al. 1973).

Spacecraft provide the most direct measurements of ULF waves, and have shown that the frequencies, polarization, and growth rates of these waves are consistent with RHI linear theory (Hoppe & Russell 1983; Dorfman et al. 2017). However, these spacecraft measurements have several limitations. Single spacecraft data sets have no spatial resolution transverse to the solar wind flow, while multi-spacecraft

<sup>4</sup> Present address: Max-Planck-Institut für Plasmaphysik, Boltzmannstr. 2, D-85748 Garching, Germany

<sup>5</sup> Present address: Department of Astrophysical Sciences, Princeton University, Princeton, New Jersey 08540, USA

**Table 1**

A Comparison of Physical Parameters and Dimensionless Quantities between the Laboratory Experiments (with the 200 J Laser) and the Earth’s Quasi-parallel Foreshock

	Laboratory	Foreshock
Core Ions	He <sup>+1</sup>	p <sup>+</sup>
Beam Ions	C <sup>+2</sup> –C <sup>+5</sup>	p <sup>+</sup>
$L$ (m)	12	$>10^7$
$B_0$ (G)	300	$5 \times 10^{-5}$
$\delta_{ci}$ (m)	0.14	$10^5$
$\omega_{cc}$ (rad s <sup>-1</sup> )	$7 \times 10^5$	0.5
$v_A$ (km s <sup>-1</sup> )	100	50
$n_c$ (cm <sup>-3</sup> )	$10^{13}$	5
$v_b$ (km s <sup>-1</sup> )	400	300
$\lambda_{mfp}$ (m)	$4 \times 10^3$	$10^{13}$
$n_b/n_c$	~10%	~10%
$v_b/v_{b,th}$	~50%	~50%
$L/\delta_{ci}$	80	$>100$
$L/\lambda_{mfp}$	$3 \times 10^{-3}$	$10^{-6}$
$v_b/v_A$	4	6

**Note.**  $L$  is the system length,  $\lambda_{mfp}$  is the beam ion/core ion Coulomb mean-free path, and  $v_{b,th}$  is the beam thermal velocity. Parameters vary substantially throughout both the experiment and the foreshock, but these values are representative. Foreshock parameters are based on measurements made by the *Wind* spacecraft (Wilson 2016).

missions are limited to a small number of transverse data points. Spacecraft measurements are inherently acquired in a moving reference frame from which properties in the plasma rest frame must be derived using other measured plasma parameters, compounding measurement errors. A moving spacecraft also cannot measure changes as a function of time at a fixed location in the plasma rest frame. In situ measurements are dependent on natural environmental variations to study instabilities under different conditions, and remote shock systems such as supernova remnants (Gargaté & Spitkovsky 2011) are physically inaccessible.

Laboratory experiments can therefore complement spacecraft measurements by reproducing phenomena in a scaled system (Drake 2000; Howes 2018). Important scaling parameters for the relevant ion physics include the core ion cyclotron frequency  $\omega_{cc} = q_c B_0/m_c$  ( $q_c$  is the core ion charge) and the core ion inertial length  $\delta_{ci} = v_A/\omega_{cc}$ . Control over experimental conditions enables systematic investigation of parameter scaling (Schaeffer et al. 2015) and conditions relevant to remote space and astrophysical systems. Measurements can be taken directly in the plasma rest frame, removing frame shifting as a potential source of error. Stationary probes can observe the growth and evolution of features in time. Repeatable measurements allow for the collection of volumetric data sets with high temporal and spatial resolution (Schaeffer et al. 2018). These measurements can then be used to validate theory, benchmark simulations, and inform the interpretation of spacecraft observations.

In this Letter we describe a series of experiments at the University of California—Los Angeles (UCLA) that drive the field-parallel RHI in the laboratory for the first time. The plasmas produced in these experiments are characterized by similar dimensionless quantities as those observed in the Earth’s quasi-parallel foreshock (Table 1). We observe waves consistent with growth of the RHI and with dimensionless

frequencies ( $\omega/\omega_{cc}$ ) comparable to ULF waves observed in the terrestrial foreshock. These waves are hereafter referred to as “ULF-analog” waves, although the experimentally measured wave frequencies do not scale exactly to the foreshock because different ion species are used. We find close agreement between the measured wave spectrum and linear theory and present unprecedented high-resolution measurements of the wave’s spatial structure. Direct comparisons of both experimental and spacecraft data with simulations demonstrate that the same instability is occurring in the terrestrial foreshock and the laboratory.

## 2. Laboratory Experiments

In the experiments the RHI is produced through the interaction of a magnetized background plasma and a laser-produced plasma (LPP) beam. The background plasma is produced by the UCLA Large Plasma Device (LAPD; Gekelman et al. 2016). Two cathodes on either end of a cylindrical 1 m  $\times$  20 m vacuum chamber produce an axially symmetric, highly repeatable He<sup>+1</sup> plasma within an ambient axial magnetic field  $B_0 = 300$  G. The radial profile of the plasma density distribution is a flat-top Gaussian centered on-axis with a 20 cm flat-top width and a peak density of  $n_c \approx 10^{13}$  cm<sup>-3</sup>. The background plasma bulk velocity is negligible over the timescale of the experiment. The LPP beam is created by one of two lasers operated by the UCLA High Energy Density Plasma (HEDP) Phoenix Laser Laboratory (Niemann et al. 2012). A high-repetition rate 15 J laser (1053 nm, 15 ns, 3600 shots hr<sup>-1</sup>) is used to collect volumetric data, while a more energetic 200 J laser (1053 nm, 25 ns, 1 shot hr<sup>-1</sup>) drives higher-amplitude waves. Both lasers have an intensity on target of  $I \approx 10^{11}$ – $10^{12}$  W cm<sup>-2</sup>. For each experiment one of the two lasers is incident on a high-density polyethylene (HDPE, C<sub>2</sub>H<sub>4</sub>) target embedded in the center of the LAPD plasma. The laser spot on target defines the origin of a coordinate system with  $\hat{z}$  parallel to the background magnetic field and  $\hat{y}$  vertically parallel to the target (Figure 1(a)), and the laser pulse defines  $t = 0$ . The target is rotated and translated between shots to continuously provide a fresh surface. The resulting LPP comprises primarily carbon charge states from C<sup>+3</sup> to C<sup>+6</sup> and expands anti-parallel to the background magnetic field. Previous measurements and linear theory (Heuer et al. 2018) have shown the LPP to be sufficiently fast and dense to drive the RHI.

Although the experiment parameters are very different from the corresponding parameters in the Earth’s quasi-parallel foreshock, the dimensionless ratios of these quantities relevant to quasi-parallel shock formation are comparable (Table 1). In both cases the system length scale  $L$  is far smaller than the beam ion/core ion Coulomb mean-free path  $\lambda_{mfp}$ , so the ion dynamics are effectively collisionless. The dimensionless experiment length  $L/\delta_{ci}$  is smaller than the foreshock, but is sufficient to observe the early stages of instability growth (Weidl et al. 2016). The beam drift velocities  $v_b$ , beam thermal velocities  $v_{b,th}$ , core plasma Alfvén velocities  $v_A$ , and beam Alfvénic Mach numbers are directly comparable to foreshock conditions.

The experiment utilizes different species of core and beam ions than are found in the foreshock, which results in slightly higher-frequency waves (when normalized to  $\omega_{cc}$ ). The experimentally measured wave frequencies therefore cannot be directly scaled to foreshock parameters for comparison, even

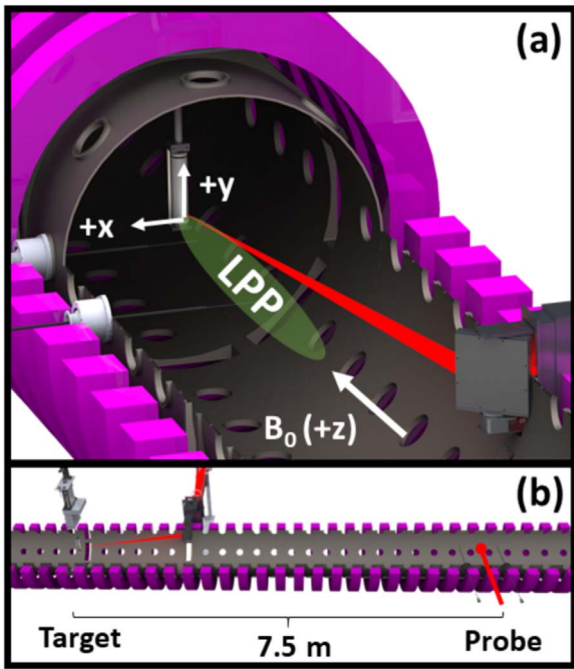


**Figure 1.** (a) The laser is directed by a steering mirror onto a plastic target embedded in the background plasma (not shown). The resulting laser-produced plasma moves anti-parallel to the background field. (b) A magnetic flux probe is positioned 7.5 m from the target.

though the same instabilities are generated. If future experiments are conducted with proton beam and core ions (a technical challenge), the results could then be directly scaled.

Magnetic fields in the experiment are measured using three-axis, 3 mm diameter magnetic flux “bdot” probes (Everson et al. 2009). Changes in the magnetic field ( $\Delta\mathbf{B}$ ) induce currents in the probes. The currents are differentially amplified, digitized, then numerically integrated to recover  $\Delta\mathbf{B}$ . Probes are positioned by motorized probe drives (Gekelman et al. 2016; resolution  $\approx \pm 0.5$  mm) and moved in 5–10 mm increments with 3–5 shots per position for statistics to compile planar data sets. All measurements reported here were made 7.5 m from the target (Figure 1(b)).

For these experimental conditions linear theory predicts a non-zero RHI growth rate (Winske & Gary 1986; Weidl et al. 2019a) and consequently the generation of dispersive right-hand circularly polarized electromagnetic waves. These waves have frequencies  $1 < \omega/\omega_{cc} < 20$  in the plasma rest frame, and wavenumbers of  $k\delta_{ci} \approx 1$ . These frequencies are higher than those observed in the foreshock ( $\omega/\omega_{cc} < 1$ ), which is predicted by theory for ions with different beam and core ion species (Winske & Gary 1986).

In accordance with theory, we have observed waves in the transverse magnetic field with maximum amplitude  $|\Delta B|/B_0 \sim 10^{-2}$  propagating with super-Alfvénic group velocity anti-parallel to the background magnetic field (Figure 2(a)). The wave polarization is determined by decomposing the transverse field components into right-hand and left-hand circularly polarized components, labeled  $B_{\text{RCP}}$  and  $B_{\text{LCP}}$ , respectively (Terasawa et al. 1986; Weidl et al. 2016) (Figure 2(b)), where right-hand circular polarization is defined by the direction of the electron cyclotron motion. The dominance of the right-hand circularly polarized component in Figure 2(b) demonstrates that the waves are right-hand circularly polarized, consistent with generation by the RHI.

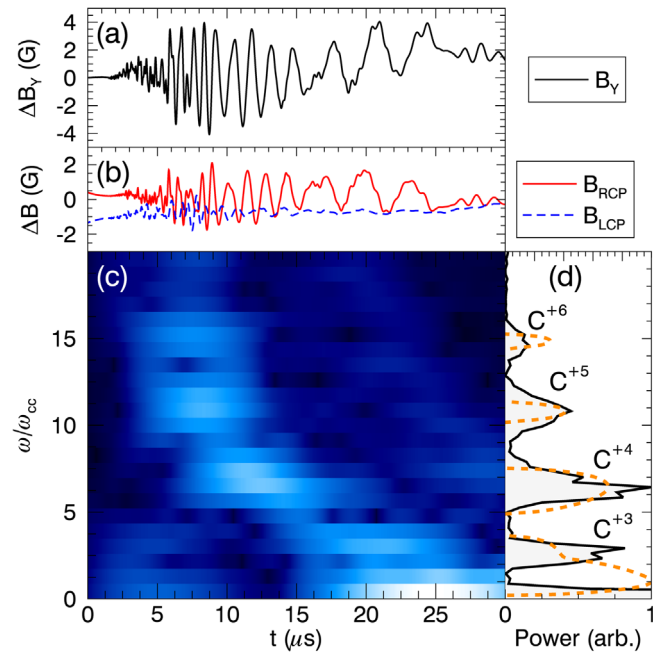


**Figure 2.** An example of oscillations observed in the transverse magnetic field measured at  $(x, y, z) = (5, 0, 750)$  cm after a shot with the 200 J laser. (a) A single measured transverse magnetic field component. (b) A polarization decomposition of the transverse field into right-hand circularly polarized (solid) and left-hand circularly polarized (dashed) components shows that the wave is dominantly right-hand circularly polarized. (c) A windowed Fourier power spectrum containing a chirp in frequency space caused by wave dispersion. (d) A Fourier transform of the entire signal (solid) shows distinct peaks in frequency corresponding to maxima in the RHI growth rate for multiple beam ion charge states (labeled  $C^{+3}$  through  $C^{+6}$ ). A calculated growth rate from linear theory (dashed) predicts peaks at frequencies corresponding to those measured. A dip in the measured spectrum at  $\omega = \omega_{cc}$  is likely due to cyclotron damping.

Spectral analysis shows that the waves fall in the predicted RHI frequency range  $1 < \omega/\omega_{cc} < 100$  (Weidl et al. 2019a) ( $\omega_{cc} \approx 100$  kHz). As expected from the linear dispersion relation (Gary 1991) the waves are dispersive, forming a frequency chirp in time (Figure 2(c)) consistent with wave growth near the target (Heuer et al. 2018).

During the experiments, multiple peaks are observed in the magnetic field frequency spectrum (Figure 2(d)). Comparison between these peaks and peaks in the growth rate predicted by multi-species linear theory for reasonable beam parameters suggests that each peak corresponds to excitation of the RHI by a different charge state of carbon (Figure 2(d), dashed line). The waves excited by each species differ in the plasma rest frame, and are further separated by Doppler shifting into the lab frame. The width of the measured peaks is larger than those predicted by the calculation, which corresponds to the non-zero width of each species’ velocity distribution.

We have used the high-repetition rate 15 J laser to map the vector magnetic field (averaged over five shots per position) in planes transverse to the background magnetic field (Figure 3(a), arrows). Neglecting the displacement current, these planes are used to calculate the field-parallel plasma current  $J_z \approx \frac{1}{\mu_0}(\nabla \times \mathbf{B})_z$  (Figure 3(a), contours). The time dependence of the transverse magnetic field and derived current from a line at  $y = 0$  are shown in Figures 3(b) and (c), respectively. Two distinct wave regimes are observed. The first, from 2 to 5  $\mu\text{s}$ , is characterized by multiple current filaments, which have also been predicted to form near the quasi-parallel



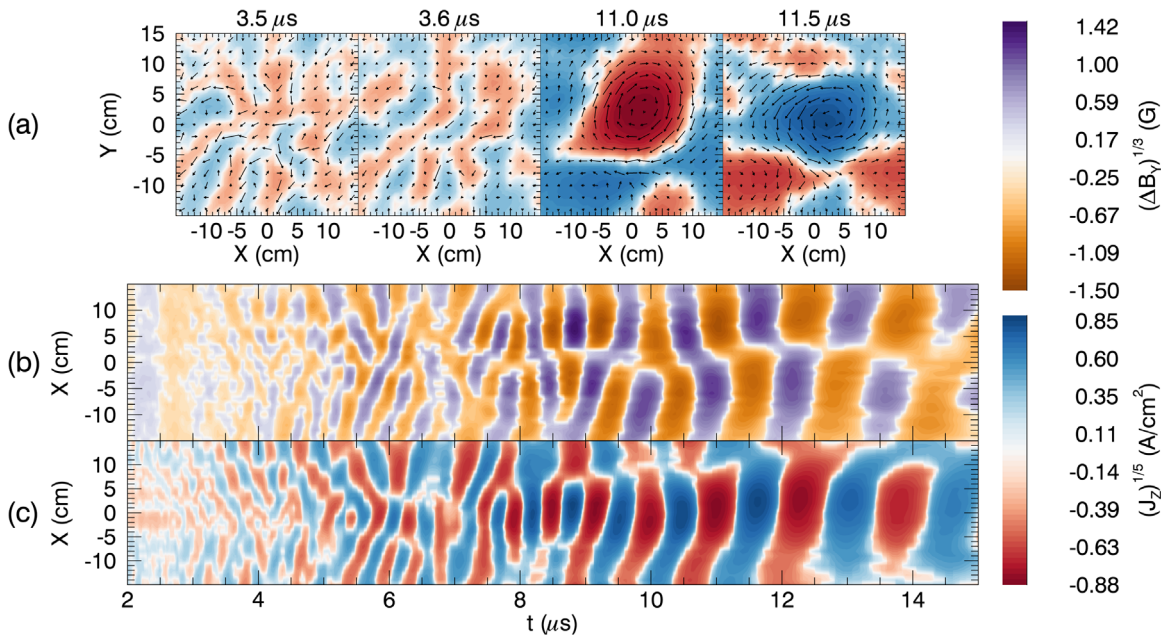


**Figure 3.** Multiple views of a transverse plane of magnetic field measurements taken 7.5 m from the target using the high-repetition rate 15 J laser. (a) Snapshots of the full transverse plane magnetic field (vectors) and calculated current (contours) in two different regimes. (b) One component of the magnetic field ( $B_y$ ) along a line through the plane at  $y = 0$  shows the wave’s temporal evolution. (c) The calculated field-aligned current along the same line as (b).

bow shock (Wang & Lin 2006; Omidi et al. 2014). As time progresses, these filaments rotate in the plane in the direction of the electron gyromotion in the lab frame. The second regime, from 8 to 14 μs, is a coherent current that oscillates along the magnetic field. Although the direction of the current structure alternates at the frequency of the wave, the magnetic field polarization of the wave at a given spatial location is always right-handed. It is notable that this type of spatial variation would be missed by single spacecraft, as time traces from opposite sides are similar except for their phase.

### 3. Comparison to Simulation and Spacecraft Measurements

Laboratory measurements can be directly compared qualitatively to spacecraft measurements, but quantitative comparison is more complicated because the carbon/helium interaction in the experiment produces waves with higher frequencies (scaled to  $\omega_{cc}$ ) than the proton/proton interaction present at the foreshock. This problem is resolved by quantitatively comparing both spacecraft and laboratory measurements to corresponding simulations. Two separate simulations, corresponding to and experiment with the 200 J laser and a small region in the terrestrial quasi-parallel foreshock, have been performed using a 2D hybrid code discussed in previous work (Weidl et al. 2016, 2017, 2019a). The 2D hybrid code models ions kinetically with a particle-in-cell approach while approximating electrons as an inertialess fluid. This approximation is valid for the frequency and length scales of interest (near  $\omega_{cc}$  and  $\delta_{ci}$ ) and makes the simulation of kinetic ion dynamics over large length scales more tractable.

The experiment simulation includes two carbon beams with different charge states ( $C^{3+}$ ,  $C^{4+}$ ) interacting with a helium background plasma (Table 1). The laser-target interaction is not simulated: instead, the LPP is initialized as it appears shortly after ablation with density velocity distributions consistent with previous characterization measurements (Schaeffer et al. 2016; Heuer et al. 2017, 2018). The simulation domain has a high

aspect ratio ( $4 \delta_{ci} \times 192 \delta_{ci}$ ) to match the experiment geometry and is described here in the same coordinate system used to describe the experiment. The spatial and temporal resolutions are  $\Delta x = \delta_{ci}/16$  and  $\Delta t = \omega_{cc}^{-1}/2000$ , respectively. The  $\pm x$  boundaries are periodic for core ions but absorb beam ions to model beam losses to the vacuum chamber walls. Beam ions that cross these boundaries are not evolved on subsequent timesteps. Periodic boundary conditions for both beam and core ions are imposed at the  $\pm z$  boundaries, although the simulation domain is chosen to be sufficiently long to prevent the fastest particles from reaching the boundary during the time range of interest. The simulation is performed in the laboratory reference frame (core ion velocity  $v_c = 0$ ).

The foreshock simulation represents a small region ( $20 \delta_{ci} \times 256 \delta_{ci}$ ) far upstream in the terrestrial quasi-parallel foreshock containing a proton beam and a proton core plasma. The simulation parameters (Table 1) are chosen to match local plasma parameters as measured by the instruments on the *Wind* spacecraft (Wilson 2016). Within this region the beam and core plasmas are assumed to be spatially uniform and all boundaries are periodic. The beam quasi-particles are initially uniformly distributed with an drifting thermal/Maxwellian velocity distribution. The spatial and temporal resolutions are  $\Delta x = \delta_{ci}/8$  and  $\Delta t = \omega_{cc}^{-1}/1000$ , respectively. The simulation is run in the spacecraft frame, in which both beam and core ions are moving to the right relative to the simulation window.

In both simulations the magnetic field at a single point is recorded at each time step to produce a time trace (Figures 4(b), (d)). The location of this “virtual probe” is arbitrary in the spatially uniform foreshock simulation, and is chosen in the experiment simulation to correspond to the real magnetic flux probe plotted in Figure 2 (and reproduced in Figure 4(a)). For comparison, a sample of ULF waves recorded by the *Wind* spacecraft (Wilson et al. 2012; Wilson 2016) on 2002 August 10 at 19:01:40 universal Time far upstream in the quasi-parallel foreshock at GSE (longitude, latitude, radius) = ( $5^\circ$ ,  $2^\circ$ ,  $20 R_E$ ), where  $R_E$  is the radius of the Earth, is plotted in Figure 4(c).

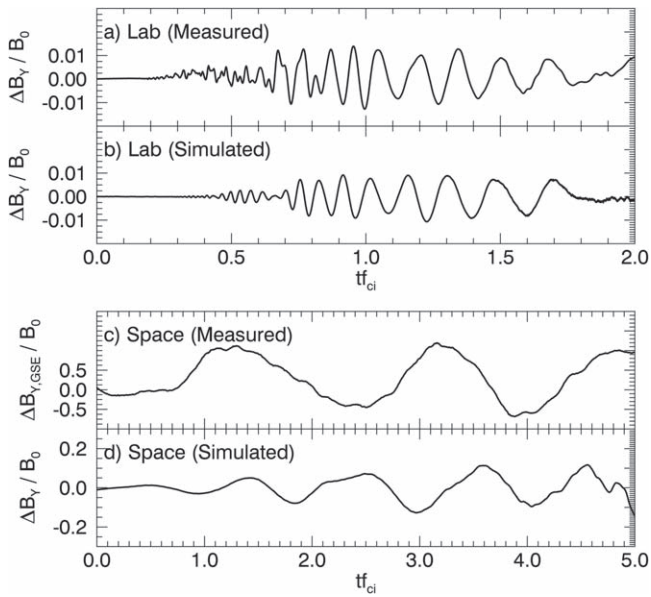


**Figure 4.** Transverse magnetic field components from the 200 J laser experiment: (a) the experiment hybrid simulation, (b) the terrestrial foreshock, (c) and the foreshock hybrid simulation (d) are scaled to their respective core ion cyclotron frequencies ( $f_{ci} = \omega_{cc}/2\pi$ ) for direct comparison. Both simulations reproduce waves similar to their respective measurements.

The waveform, frequencies, and polarization (not shown) of both the experimental data (Figure 4(a)) and the spacecraft measurements (Figure 4(c)) are well reproduced by their respective simulations. Some of the highest frequency waves observed in the experiment ( $\omega \gtrsim 15 \omega_{cc}$ ) are not resolved by the hybrid simulation, which explains the absence of the waves with the earliest arrival times in Figure 4(b). The waves observed in the foreshock reach much larger (highly nonlinear) amplitudes relative to  $B_0$  than the experimentally observed waves, likely due to a combination of longer growth times and faster beam ions. The foreshock simulation reaches larger amplitudes than the experiment, but also saturates before matching the spacecraft-measured amplitude at a level determined by the starting energy of the system: in the foreshock inflowing particles contribute additional energy, but incorporating these particles in the simulation presents challenges outside the scope of this work. The waveform, polarization, and frequency agreement between measurements and simulation validates the hybrid model, and suggests that the same ion-driven physical process responsible for creating ULF waves in the foreshock, i.e., the RHI, is responsible for creating the waves observed in the laboratory.

#### 4. Conclusion

In summary, ULF-analog waves driven by the field-parallel RHI have been produced in the laboratory for the first time. These waves are created using an experimental platform at UCLA that combines one of two high-energy lasers with the magnetized ambient background plasma of the Large Plasma Device (LAPD). The experiment is characterized by dimensionless quantities comparable to the terrestrial quasi-parallel foreshock, although the wave frequencies do not scale exactly because different ion species are used. The waves are observed with a magnetic flux probe and found to be consistent with linear theory for the RHI. Novel volumetric measurements using a high-repetition rate laser reveal the spatial structure of

these waves, including evidence of current filaments. Experimental data and spacecraft observations contain similar waves, and the frequencies of both are quantitatively well matched by corresponding 2D hybrid simulations. These results show that ULF-analog waves can be successfully produced in the laboratory by the same mechanism that creates ULF waves in space.

The creation of beam instabilities and waves in the laboratory analogous to those observed in the terrestrial foreshock allows control over experimental conditions and unprecedented validation of simulation and theoretical models in three dimensions. Spacecraft have a limited ability to study the temporal evolution or transverse spatial features of phenomena, and are therefore complemented by laboratory measurements of this type. Future work will investigate current filamentation, large-amplitude waves with nonlinear effects, and other ion beam instabilities with the goal of better understanding the formation and properties of parallel collisionless shocks.

This work was supported by the Defense Threat Reduction Agency, Lawrence Livermore National Security LLC, and the Department of Energy (DOE) under contract No. DE-SC0017900. The Peening laser was made available by the Naval Information Warfare Center Pacific under contract No. NCRADA-NIWC Pacific-19-354. L.B.W.'s work was partially supported by the International Space Science Institute's International Teams programme, *Wind* MO&DA funds, and a Heliophysics Innovation Fund, and M.S.W. was partially supported by the Deutsche Forschungsgemeinschaft. The experiments were performed at the UCLA Basic Plasma Science Facility (BaPSF), which is a collaborative research facility supported by the U. S. Department of Energy, Office of Science, Office of Fusion Energy Sciences, and the National Science Foundation. We would like to thank the staff of BaPSF, Z. Lucky, M. Drandell, T. Ly, and A. Kohli for their help conducting the experiments.

#### ORCID iDs

Peter V. Heuer <https://orcid.org/0000-0001-5050-6606>

Lynn B. Wilson III <https://orcid.org/0000-0002-4313-1970>

#### References

- Akimoto, K., Gary, S. P., & Omid, N. 1987, *JGR*, **92**, 11209
- Blandford, R., & Eichler, D. 1987, *PhR*, **154**, 1
- Burgess, D. 1989, *GeoRL*, **16**, 345
- Burgess, D. 1995, *AdSpR*, **15**, 159
- Burgess, D., Möbius, E., & Scholer, M. 2012, *SSRv*, **173**, 5
- Burgess, D., & Scholer, M. 2012, *SSRv*, **173**, 5
- Caprioli, D., & Spitkovsky, A. 2014, *ApJ*, **783**, 91
- Dorfman, S., Hietala, H., Astfalk, P., & Angelopoulos, V. 2017, *GeoRL*, **5**, 2120
- Drake, R. P. 2000, *PhPI*, **7**, 4690
- Eastwood, J. P., Lucek, E. A., Mazelle, C., et al. 2005, *SSRv*, **118**, 41
- Everson, E. T., Pribyl, P., Constantin, C. G., et al. 2009, *RSci*, **80**, 113505
- Fuselier, S. 1995, *AdSpR*, **15**, 43
- Gargaté, L., & Spitkovsky, A. 2011, *ApJ*, **744**, 67
- Gary, S. P. 1991, *SSRv*, **56**, 373
- Gekelman, W., Pribyl, P., Lucky, Z., et al. 2016, *RSci*, **87**, 025105
- Golden, K. I., Linson, L. M., & Mani, S. A. 1973, *PhFI*, **16**, 2319
- Greenstadt, E., Le, G., & Strangeway, R. 1995, *AdSpR*, **15**, 71
- Hada, T., Kennel, C. F., & Terasawa, T. 1987, *JGR*, **92**, 4423
- Heuer, P., Schaeffer, D., Knall, E., et al. 2017, *HEDP*, **22**, 17
- Heuer, P. V., Weidl, M. S., Dorst, R. S., et al. 2018, *PhPI*, **25**, 032104
- Hoppe, M., & Russell, C. 1981, *AdSpR*, **1**, 327

- Hoppe, M. M., & Russell, C. T. 1983, *JGRA*, **88**, 2021
- Hoppe, M. M., Russell, C. T., Eastman, T. E., & Frank, L. A. 1982, *JGR*, **87**, 643
- Howes, G. G. 2018, *PhPI*, **25**, 055501
- Jeffrey, H. W. 2013, in *Solar Wind Sources of Magnetospheric Ultra-Low-Frequency Waves*, ed. M. J. Engebreston, K. Takahashi, & M. Scholer (Washington, DC: AGU), 1
- Montgomery, M. D., Gary, S. P., Forslund, D. W., & Feldman, W. C. 1975, *PhRvL*, **35**, 667
- Niemann, C., Constantin, C. G., Schaeffer, D. B., et al. 2012, *JInst*, **7**, P03010
- Omidi, N., Sibeck, D., Gutynska, O., & Trattner, K. J. 2014, *JGRA*, **119**, 2593
- Onsager, T. G., Winske, D., & Thomsen, M. F. 1991, *JGR*, **96**, 1775
- Schaeffer, D. B., Bondarenko, A. S., Everson, E. T., et al. 2016, *JAP*, **120**, 043301
- Schaeffer, D. B., Everson, E. T., Bondarenko, A. S., et al. 2015, *PhPI*, **22**, 113101
- Schaeffer, D. B., Hofer, L. R., Knall, E. N., et al. 2018, *JPhCS*, **388**, 152022
- Scholer, M., & Burgess, D. 1992, *JGR*, **97**, 8319
- Terasawa, T., Hoshino, M., Sakai, J., & Hada, T. 1986, *JGR*, **91**, 4171
- Tsurutani, B. T. 2013, *GMS*, **61**, 189
- Turner, D. L., Wilson, L. B., Liu, T. Z., et al. 2018, *Natur*, **561**, 206
- Wang, X. Y., & Lin, Y. 2006, *PhPI*, **13**, 052102
- Weidl, M. S., Heuer, P., Schaeffer, D., et al. 2017, *JPhCS*, **900**, 012020
- Weidl, M. S., Winske, D., Jenko, F., & Niemann, C. 2016, *PhPI*, **23**, 122102
- Weidl, M. S., Winske, D., & Niemann, C. 2019a, *ApJ*, **873**, 57
- Weidl, M. S., Winske, D., & Niemann, C. 2019b, *ApJ*, **872**, 48
- Wilson, L. B., Koval, A., Szabo, A., et al. 2012, *GeoRL*, **39**, L08109
- Wilson, L. B., III 2016, in *Low-Frequency Waves in Space Plasmas*, ed. A. Keiling, D.-H. Lee, & V. Nakariakov (New York: Wiley), 269
- Winske, D., & Gary, S. P. 1986, *JGR*, **91**, 6825
- Winske, D., Omidi, N., Quest, K. B., & Thomas, V. A. 1990, *JGR*, **95**, 18821